



# One-pot synthesis of atomically dispersed Pt on MnO<sub>2</sub> for efficient catalytic decomposition of toluene at low temperatures

Huiyu Zhang<sup>a</sup>, Shanhong Sui<sup>a</sup>, Xianming Zheng<sup>a</sup>, Ranran Cao<sup>a</sup>, Pengyi Zhang<sup>a,b,\*</sup>

<sup>a</sup> State Key Joint Laboratory of Environment Simulation and Pollution Control, School of Environment, Tsinghua University, Beijing, 100084, China

<sup>b</sup> Beijing Key Laboratory for Indoor Air Quality Evaluation and Control, Beijing, 100084, China

## ARTICLE INFO

### Keywords:

Single atom  
Catalytic oxidation  
Manganese dioxide  
Toluene  
Indoor air purification

## ABSTRACT

The catalytic degradation of volatile organic compounds (VOCs) at low temperature is still a great challenge for indoor air purification. In this paper, the doping of single-atom Pt into MnO<sub>2</sub> with a one-pot hydrothermal process greatly improved the catalytic activity for toluene degradation at room temperature, achieving 100% conversion of 0.42 ppm toluene at 28 °C under the high gas-hourly-space-velocity of 300 L g<sup>-1</sup> h<sup>-1</sup>. Furthermore, it achieved 100% conversion of 10 ppm toluene at 80 °C and complete oxidation into CO<sub>2</sub> at 220 °C. The manganese and oxygen defects in MnO<sub>2</sub> nanosheets effectively stabilized the single-atom platinum, and strong oxidative hydroxyl radicals (<sup>•</sup>OH) is thought to contribute to its excellent performance.

## 1. Introduction

Indoor air quality directly affects people's health, and recently gets growing attention all over the world especially in the developing countries. Long-term exposure to multi-component volatile organic compounds (VOCs), such as formaldehyde, hexanal, benzene, toluene and many other low-concentration pollutants, would stimulate the eyes, skin and respiratory tract, and even cause irreversible damage to human health [1–4]. In the past decade, significant progress has been achieved in catalytically decomposing formaldehyde (HCHO) into carbon dioxide at room temperature by noble metal and manganese dioxide [5–10]. However, effective and economical decomposition of longer carbon-chain VOCs such as toluene and hexanal still faces great challenges in the practical indoor air purification. Many methods have been tried, including photocatalysis [11,12], non-thermal plasma catalysis [13] and thermal catalysis. Thermal catalytic oxidation by supported noble metals is considered as one of the effective and simple methods to decompose VOCs at low temperatures [14,15]. However, the high cost inhibits the wide application of noble-metal catalysts. The recent explosive growth in research on single-atom catalysts (SACs) offers a great potential to significantly increase the catalytic activity using less amount of noble metals [16].

The isolated noble-metal single atom usually has high surface energy, quantum size effect, unsaturated coordination environment and metal-carrier interaction, which make the single-atom catalysts

showing excellent catalytic activity and selectivity [16–19]. SACs have showed great potential in a variety of catalytic reactions, such as CO oxidation [19–21], formaldehyde oxidation at ambient temperature [9], water-gas-shift reactions [22,23], and selective electrochemical reactions [24,25], and so on. Lots of experiments have shown that the turnover frequency (TOF) per atom is improved by several orders of magnitude higher than that of nanocluster [16,26]. However, when the particle size reduces to the atomic level, the noble metal atoms tend to aggregate into nanoclusters during the material preparation process or in the catalytic reaction due to their high surface energy and mobility [16]. Therefore, how to conveniently and effectively prepare single-atom catalysts and maintain their stability and high efficiency during reaction is still a great challenge. Qiao et al. [19] used sodium carbonate to improve the atomic dispersion of Pt on the surface of FeOx support, which showed extremely high atom efficiency and excellent stability for CO oxidation. Zhang et al. [9] also found that the addition of alkali-metal ions (Li<sup>+</sup>, Na<sup>+</sup>, and K<sup>+</sup>) stabilized an atomically dispersed Pt on TiO<sub>2</sub>, significantly promoting the activity for the HCHO oxidation at ambient temperature. Wan et al. [21] reported that surface defects on supports such as TiO<sub>2</sub> could effectively stabilize single atomic Au and promote the catalytic properties through reducing the energy barrier and relieving the competitive adsorption on isolated atomic sites. Hence, the selection of appropriate support is key to develop single atom catalysts preventing aggregation of isolated single atoms.

\* Corresponding author at: State Key Joint Laboratory of Environment Simulation and Pollution Control, School of Environment, Tsinghua University, Beijing, 100084, China.

E-mail address: [zpy@tsinghua.edu.cn](mailto:zpy@tsinghua.edu.cn) (P. Zhang).

<https://doi.org/10.1016/j.apcatb.2019.117878>

Received 21 March 2019; Received in revised form 23 May 2019; Accepted 17 June 2019

Available online 19 June 2019

0926-3373/ © 2019 Elsevier B.V. All rights reserved.

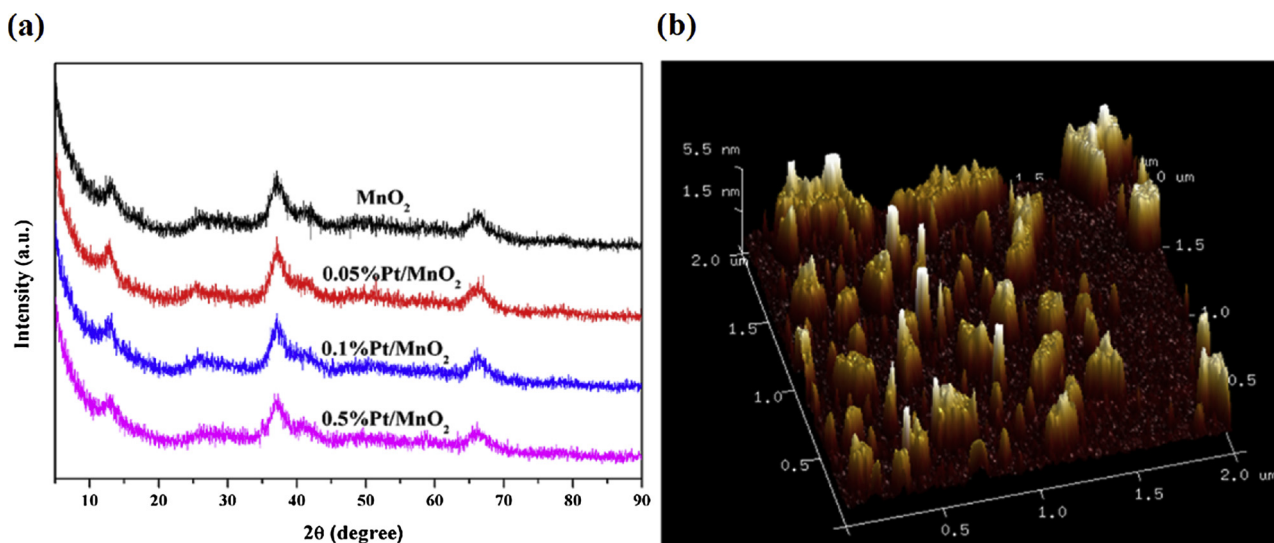


Fig. 1. (a) XRD patterns of as-synthesized MnO<sub>2</sub> and atomically Pt deposited MnO<sub>2</sub> samples with different Pt loadings; (b) Tapping-mode AFM image of ultrathin 0.1%Pt/MnO<sub>2</sub> nanosheets.

Manganese oxide has been widely studied due to its excellent catalytic properties [5–8,27,28]. Ultrathin birnessite-type MnO<sub>2</sub> nanosheets showed high activity toward ppm-level HCHO into harmless CO<sub>2</sub> at room temperature [5]. There are lots of defects such as Mn and O vacancies, abundant surface hydroxyl groups and interlayer cations in the MnO<sub>2</sub> structure, which have a close relationship with its excellent catalytic activity [6,6,7,8]. In addition, there are lots of research about combination of manganese dioxide with TiO<sub>2</sub>, CeO<sub>2</sub> and precious metals, which usually displayed excellent catalytic performance [29–31]. For instance, MnOx supported on activated carbon (AC) with SiO<sub>2</sub> encapsulated modification could efficiently catalyze the complete transformation of benzene into CO<sub>2</sub> by ozone at ambient temperature [29]. Thus, MnO<sub>2</sub> and its derivative has been widely used in the catalytic oxidation of VOCs [27–29,32], ozone decomposition [33,34] and supercapacitor [35,36] etc.

In this study, we made use of the structure defects in MnO<sub>2</sub> to strongly anchor single-atom Pt into the ultrathin MnO<sub>2</sub> nanosheet by a simple one-pot hydrothermal method. High-angle annual dark-filed scanning transmission electron microscopy (HAADF-STEM) and XAFS analysis showed that platinum was atomically dispersed in the MnO<sub>2</sub> structure. As-prepared single-atom Pt deposited MnO<sub>2</sub> showed excellent activity for toluene oxidation. This work initiates a new method to develop single-atom noble metal catalysts for VOCs degradation.

## 2. Experimental section

### 2.1. Catalyst preparation

All chemicals were of analytical grade and used as received without further purification. MnO<sub>2</sub> nanosheets with different loading of platinum were synthesized via a hydrothermal process. Briefly, 3.16 g potassium permanganate (KMnO<sub>4</sub>), 1.42 g (NH<sub>4</sub>)<sub>2</sub>C<sub>2</sub>O<sub>4</sub>·H<sub>2</sub>O were dissolved in 70 mL deionized water with magnetic stirring. Subsequently, aqueous solution of chloroplatinic acid (H<sub>2</sub>PtCl<sub>6</sub>) was added in and magnetically stirred for 10 min. Then the above mixed solution was transferred into a 100 mL Teflon-lined stainless-steel autoclave. The autoclave was heated to 90 °C in an electric oven and maintained for 24 h. After the autoclave naturally cooled down to the room temperature, the precipitates were collected by centrifugation and washed with deionized water for several times. Then, the solid products were dried at 105 °C in air for 12 h. Finally, the samples were calcined at 180 °C in a flow of 100 mL min<sup>−1</sup> 10% H<sub>2</sub>/N<sub>2</sub> for 1 h. The obtained powders were denoted as MnO<sub>2</sub>, 0.05%Pt/MnO<sub>2</sub>, 0.1%Pt/MnO<sub>2</sub> and 0.5%Pt/MnO<sub>2</sub>

respectively depending on the nominal weight ratio of Pt/Mn.

### 2.2. Characterization

Morphology observation was recorded on a Hitachi S5500 field-emission scanning electron microscope (Hitachi Co., Ltd., Japan) operated at 5 kV. TEM images were obtained on a JEM-2011 transmission electron microscope (JEOL, Japan) operated at 150 kV. High-angle annual dark-filed scanning transmission electron microscopy (HAADF-STEM) images were obtained on a Titan Cubed Themis 60–300, the gun type was X-FEG with monochromator, the electron energy loss spectrometry type was Gatan Quantum 965 Spectrometer, the guaranteed resolution is 0.06 nm. The crystal structures of samples were verified by a Bruker X-ray diffraction instrument (Model D8-Avance, Bruker, Germany) with a Cu Kα X-ray source. Atomic force microscopy (AFM) images of samples were carried out in tapping mode with a Bruker Dimension ICON. X-ray photoelectron spectroscopy (XPS) was measured by ESCALAB 250Xi (Thermo Fisher, USA) equipped with an Al Kα X-ray source. The binding energy was corrected by referring to the C 1s peak at 284.8 eV. The surface area was determined on a Micromeritics ASAP 2020 nitrogen adsorption apparatus (USA) by Brunauer–Emmett–Teller (BET) model. The content of platinum was determined by inductively coupled plasma/optical emission spectroscopy (ICP-OES, Thermo IRIS Intrepid II XSP) after the sample was dissolved by acid. Electronic spinning resonance (ESR) analysis were conducted on a Bruker EPR 300E spectrometer using 5,5-dimethyl-1-pyrroline N-oxide (DMPO) as trapping agent in aqueous suspension.

H<sub>2</sub> temperature programmed reduction (H<sub>2</sub>-TPR) profiles were obtained in a Micromeritics AutoChem II 2920 instrument equipped with a thermal conductivity detector (TCD). 50 mg catalyst was heated to 105 °C and purged with He gas (50 ml min<sup>−1</sup>) for 0.5 h. After it cooled to room temperature, the catalyst was heated in 5% H<sub>2</sub>/Ar (50 ml min<sup>−1</sup>) from 40 °C to 600 °C at a heating rate of 5 °C min<sup>−1</sup>. The O<sub>2</sub>-TPD was also carried out with the same instrument. 50 mg sample was first purged with He at 105 °C for 30 min. Then, the catalyst was purged with O<sub>2</sub> (50 ml min<sup>−1</sup>) at room temperature. After that, the sample was purged with He (50 ml min<sup>−1</sup>) for 30 min to remove the physisorbed O<sub>2</sub> and stabilize the detector baseline. Finally, the temperature rose from 30 °C to 950 °C at a ramp of 5 °C min<sup>−1</sup> in the He stream.

Diffuse reflectance infrared Fourier transform spectrometry (DRIFTS) was collected on a Nicolet 6700 FTIR (Thermo Fisher, USA) equipped with an *in-situ* cell to detect the surface intermediate formed during toluene oxidation. The samples were pretreated by N<sub>2</sub> (30 mL

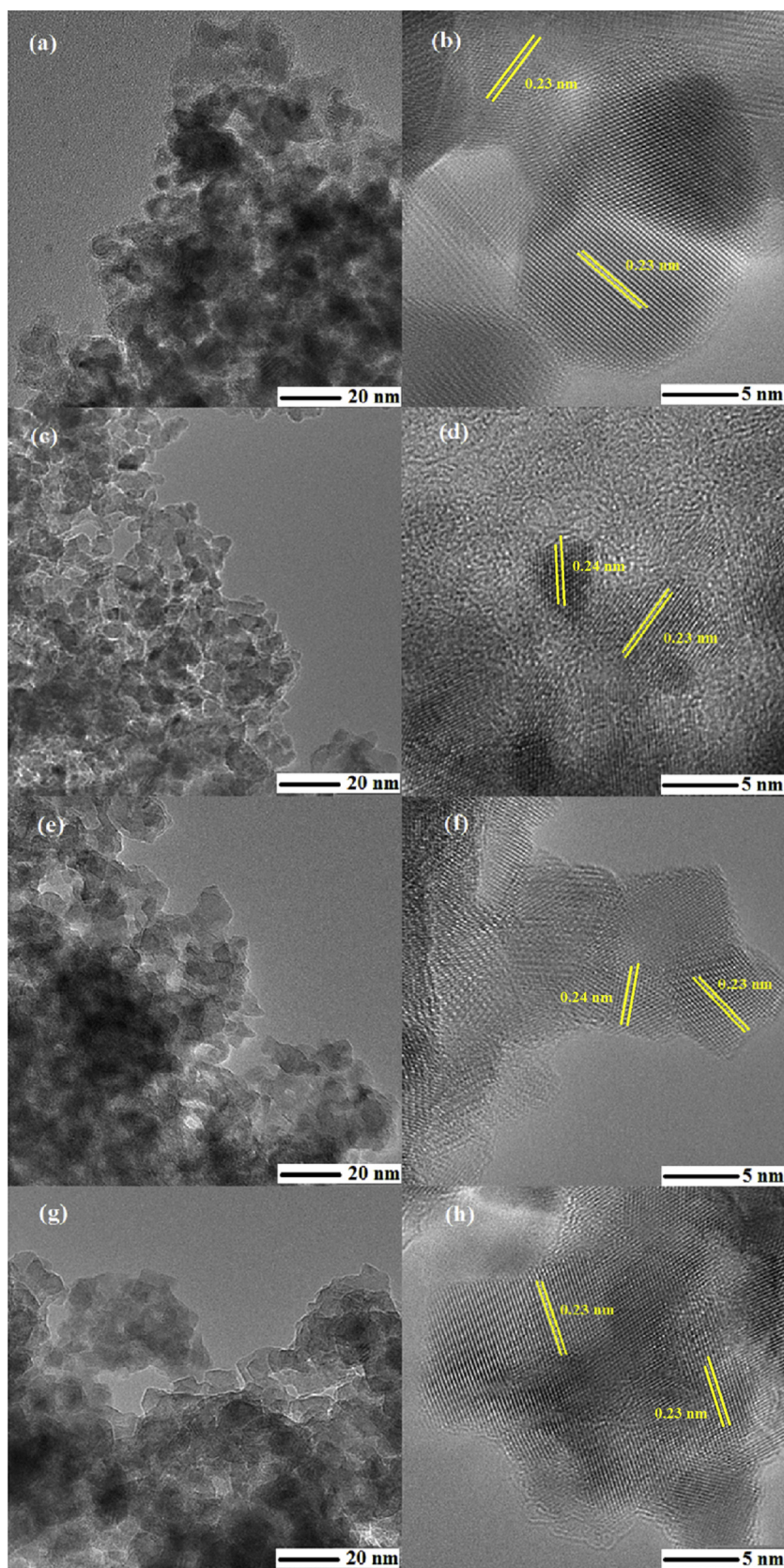


**Fig. 2.** TEM and HRTEM images. (a, b) MnO<sub>2</sub> (c, d) 0.05%Pt/MnO<sub>2</sub>, (e, f) 0.1%Pt/MnO<sub>2</sub>, (g, h) 0.5%Pt/MnO<sub>2</sub>.

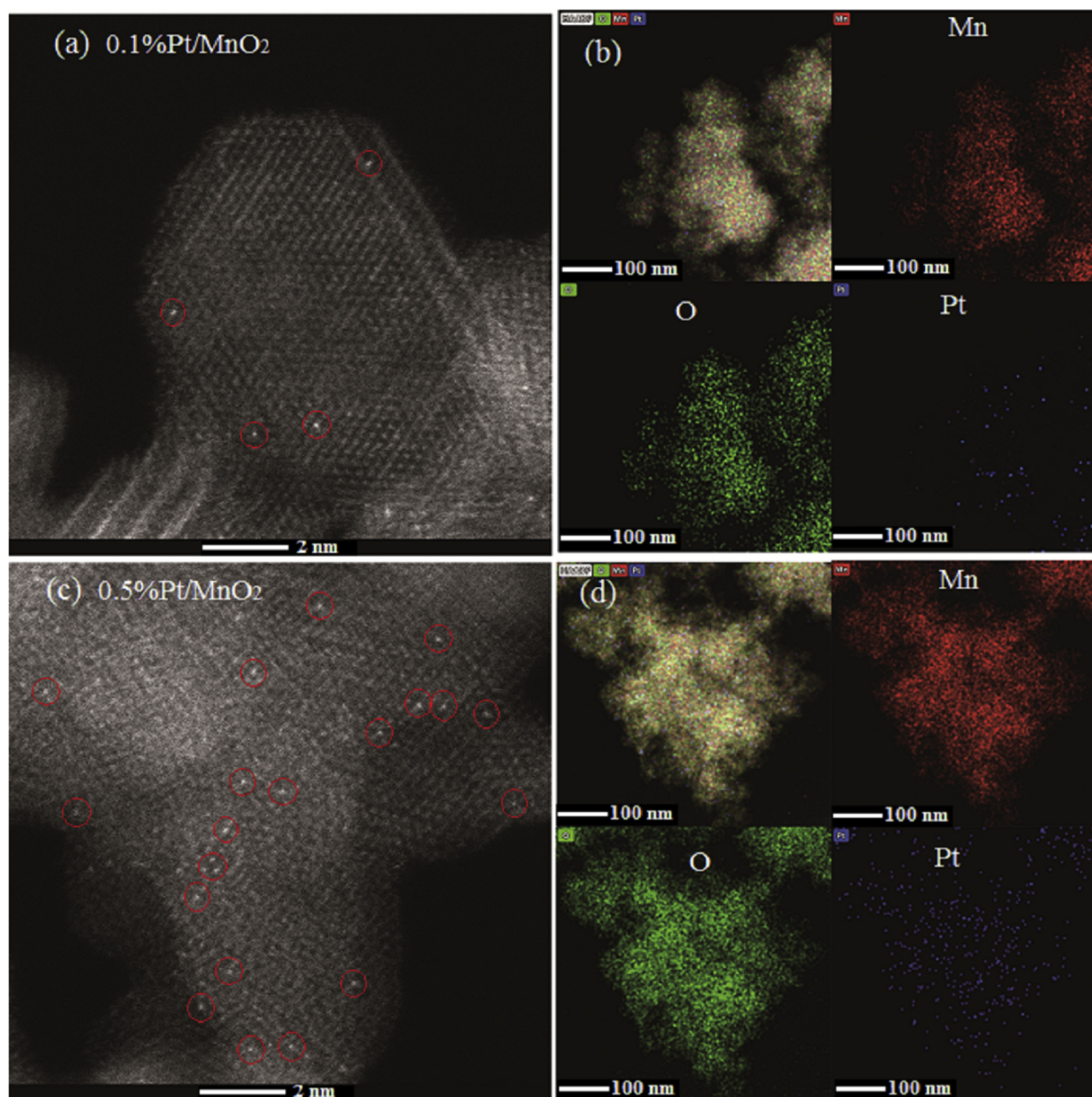


Fig. 3. High-angle annular dark-field STEM images and STEM-EDS images with element distribution images. (a, b) 0.1%Pt/MnO<sub>2</sub>; (c, d) 0.5%Pt/MnO<sub>2</sub>.

Table 1

ICP, BET surface area and XPS results of different samples.

Sample	Pt (ICP, wt%)	BET (m <sup>2</sup> g <sup>-1</sup> )	Pore Volume (cm <sup>3</sup> g <sup>-1</sup> )	AOS	Mn/O	XPS O <sub>ads</sub> /O <sub>latt</sub>	Mn <sup>3+</sup> /Mn <sup>4+</sup>	TOF 28 °C (s <sup>-1</sup> )
MnO <sub>2</sub>	0	125.0	0.25	3.10	1.41:2	0.31	1.95	–
0.05%Pt/MnO <sub>2</sub>	0.042	142.7	0.28	3.17	1.32:2	0.35	1.48	0.21
0.1%Pt/MnO <sub>2</sub>	0.081	104.9	0.20	3.21	1.31:2	0.37	1.30	0.15
0.5%Pt/MnO <sub>2</sub>	0.41	88.2	0.22	3.33	1.20:2	0.44	1.15	0.025

min<sup>-1</sup>) at the designed temperature for 1 h, then 15 ppm of toluene was injected at a flow rate of 30 mL min<sup>-1</sup> with the synthetic air as the balance gas at the designed temperature.

The extended X-ray Absorption Fine Structure (EXAFS) analysis of the Mn-K and Pt-L<sub>III</sub> edges were respectively measured in transmission and fluorescence mode at Beijing Synchrotron Radiation Facility

(BSRF). The X-ray absorption edge energy was calibrated with Mn foil at 6539 eV and Pt foil at 11,564 eV, respectively. The data were analyzed using the Athena program.

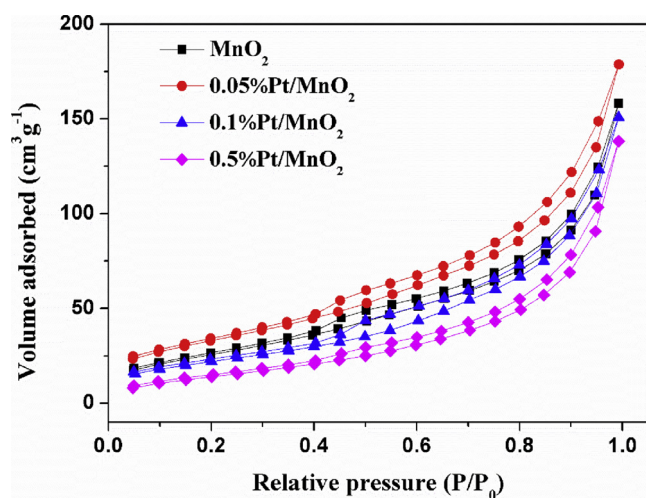


Fig. 4. N<sub>2</sub> adsorption-desorption isotherms of four catalysts.

### 2.3. Catalytic activity tests

The catalytic performance for the toluene oxidation were investigated in a fixed-bed quartz tube reactor (i.d. = 6 mm). 100 mg samples with the size of 40–60 meshes were loaded in the reactor which was placed in a pipe furnace. The reaction temperature was controlled and maintained for 1 h at each designed temperature before it decreased to the next designed temperature. The inlet toluene concentration was set at 10 ppm, and the total flow rate of was 100 mL min<sup>-1</sup> with the corresponding gas hourly space velocity (GHSV) of 60 L g<sup>-1</sup> h<sup>-1</sup>. The concentrations of toluene and generated CO<sub>2</sub> were determined by GC-2014 (Shimadzu, Japan) equipped with a flame ionization detector (FID) and a methanizer. The toluene conversion ratio was calculated as follows:

$$\text{Toluene conversion (\%)} = \left(1 - \frac{C_{\text{out}}}{C_{\text{in}}}\right) \times 100\%$$

where  $C_{\text{in}}$  and  $C_{\text{out}}$  are the molar concentration of toluene in the inlet and outlet, respectively. And the conversion of toluene into CO<sub>2</sub> was calculated as follows:

$$\text{CO}_2 \text{ conversion (\%)} = \frac{[\text{CO}_2]_{\text{out}}}{7 \times C_{\text{in}}} \times 100\%$$

where  $[\text{CO}_2]_{\text{out}}$  is the molar concentration of CO<sub>2</sub> in the outlet.

The performance of 0.1%Pt/MnO<sub>2</sub> catalyst was also tested for low concentration toluene (0.42 ppm) at room temperature (28 °C) in the same reactor under the GHSV of 300 L g<sup>-1</sup> h<sup>-1</sup>, and for high concentration toluene (100 ppm) under the GHSV of 48 L g<sup>-1</sup> h<sup>-1</sup>.

## 3. Results and discussion

### 3.1. Crystal structure and textural properties

Birnessite MnO<sub>2</sub>, composed of edge-sharing octahedral MnO<sub>6</sub>, is a kind of layered transition metal oxides. It is common to form manganese defects and oxygen vacancies during the crystallization process [6–8,37]. In this study, we managed to utilize the Mn vacancy to disperse single-atom Pt on MnO<sub>2</sub> by a simple one-pot hydrothermal process. Fig. 1a shows the XRD patterns of pure MnO<sub>2</sub> and three Pt-deposited MnO<sub>2</sub> samples with different Pt loadings. Four weak diffraction peaks centered at 12.3°, 24.6°, 36.5° and 65.5° can be assigned to the birnessite-type MnO<sub>2</sub> (JCPDS No. 80-1098) with poor crystallinity. And no peaks ascribed to Pt or PtO<sub>2</sub> were observed. These four samples showed very similar diffraction patterns, which indicate the deposition of small amount of Pt did not obviously change the crystal structure of MnO<sub>2</sub>. The structure of 0.1%Pt/MnO<sub>2</sub> nanosheets was also confirmed

by the tapping-mode AFM image in Fig. 1b. The thickness of the nanosheets were approximate 2–6 nm, suggesting a successful synthesis of ultrathin MnO<sub>2</sub> nanosheet.

TEM images (Fig. 2a, c, e, g) show the similar morphologies of MnO<sub>2</sub> and Pt-deposited MnO<sub>2</sub>, all these samples consisted of nanosheets with the planar size of ~10 nm. And no Pt clusters or particles could be observed. From the HRTEM images (Fig. 2b, d, f, h), the fuzzy lattice spacing of 0.23 and 0.24 nm could be identified, which correspond to the {1 1 1} and {-1 1 1} facets of birnessite MnO<sub>2</sub> [7] and further confirmed the poor crystallinity as reflected by XRD patterns. Furthermore, it can be seen in Fig. 2d, f and h, after deposited with Pt, the lattice fringe became more obscure with some obvious amorphous areas. To know the dispersion of Pt on MnO<sub>2</sub>, high-angle-annular-dark-field scanning transmission electron microscopy (HAADF-STEM) was performed. It could be clearly observed in Fig. 3a and c that a lot of bright points dispersed on MnO<sub>2</sub> nanosheets, indicating the atomically dispersion of Pt atoms on the MnO<sub>2</sub> support. The EDS mapping suggest the uniform distribution of Pt atoms over the entire architecture (Fig. 3b and d).

To explore the physicochemical properties of as-prepared catalysts, ICP-OES, BET and XPS analysis were carried out to check the effect of the amounts of Pt. ICP-OES results revealed the actual loading of Pt deposited on MnO<sub>2</sub>. As shown in Table 1, the actual amounts of Pt were almost 80% of the nominal Pt in all three Pt-deposited MnO<sub>2</sub> samples, indicating most Pt were deposited on the MnO<sub>2</sub> even when the nominal Pt amount was as high as 0.5%. As indicated by TEM observation in Fig. 2, when a small amount of platinum was deposited, the structure of manganese dioxide nanosheet was distorted with increasing of amorphous area. Correspondingly, as shown in Table 1, the specific surface area was increased a little from 125 to 142.7 m<sup>2</sup> g<sup>-1</sup>, which was calculated from the nitrogen adsorption/desorption curves (Fig. 4). As can be seen in Table 1, when the Pt content further increased, the specific surface area decreased from 142.7 to 104.9 and 88.2 m<sup>2</sup> g<sup>-1</sup>. We think this phenomenon can be ascribed to the aggregation of MnO<sub>2</sub> nanosheets due to its high specific surface energy caused by the atomically doping of Pt atoms [16,19]. To reduce the surface energy, the MnO<sub>2</sub> nanosheets tend to aggregate. However, though MnO<sub>2</sub> nanosheets aggregated to some extent, the Pt atoms still are atomically dispersed in the MnO<sub>2</sub> crystal as seen in Fig. 3.

XPS analysis was conducted to explore the surface chemical states. The average oxidation state (AOS) of manganese atoms were calculated according to the binding energy difference between characteristic peaks of Mn 3s patterns (Fig. 5a) [8]. As listed in Table 1, the AOS value 3.10 of Mn in MnO<sub>2</sub> was much lower than frequently reported value of MnO<sub>2</sub>, which could be ascribed to the hydrogen treatment at 180 °C during catalyst preparation. With the deposition of Pt, the AOS value obviously increased to 3.33 in the 0.5%Pt/MnO<sub>2</sub> sample. Furthermore, with the increase of deposited Pt, the Mn/O ratio decreased, indicating the content of Mn decreased. With the XPSPEAK41 software, the Mn 2p peak was deconvoluted into two peaks (Fig. 5b), which were assigned to the Mn<sup>3+</sup> (638 eV–644 eV) and Mn<sup>4+</sup> (640 eV–646 eV), respectively. As shown in Table 1, most manganese atoms existed in the form of Mn<sup>3+</sup>, which was consist with the results of AOS, indicating there were a lot of oxygen vacancies on the surface of MnO<sub>2</sub>. The O 1s spectra of different samples are shown in Fig. 5c. The binding energy located at 528.0–530.5 and 529.5–532.5 eV were assigned to the lattice oxygen (O<sub>latt</sub>) and the surface adsorbed oxygen species (O<sub>ads</sub>), respectively [8]. With the increase of deposited Pt amount, the ratio of O<sub>ads</sub>/O<sub>latt</sub> increased from 31% to 44%, implying that much more adsorbed oxygen species existed on the surface of the catalyst. Fig. 5d shows the Pt 4f spectrum of the catalyst. According to the fitting data of 0.5%Pt/MnO<sub>2</sub> sample as shown in Fig. 5e, we can find that Pt atoms exist in two chemical states at binding energies of 74.9 eV and 73.3 eV, respectively, with the spin-orbit split doublets at 3.45 eV higher for each peak. The peak at 74.9 eV corresponding to Pt<sup>4+</sup> contributed major to the spectrum, indicating deposited Pt atoms mainly existed in the form of Pt<sup>4+</sup>.

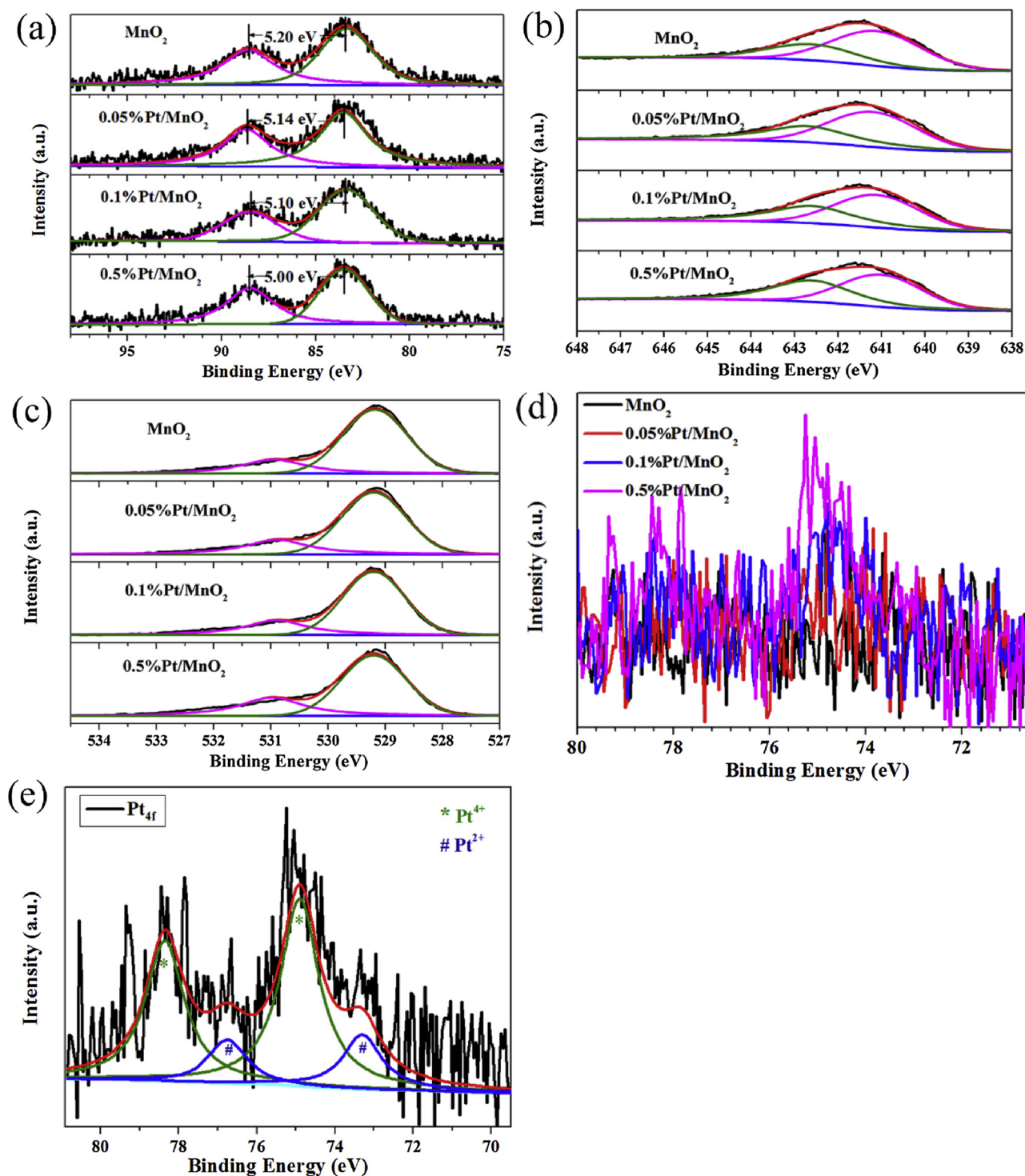


Fig. 5. XPS spectra of (a) Mn 3s, (b) Mn 2p, (c) O 1s, (d) Pt 4f of different Pt-deposited MnO<sub>2</sub> samples, (e) Pt 4f fitting patterns of 0.5%Pt/MnO<sub>2</sub>.

The small peak at 73.3 eV corresponding to Pt<sup>2+</sup> [38,39]. The area ratio of Pt<sup>2+</sup>/Pt<sup>4+</sup> was 0.3, indicating that deposited Pt<sup>4+</sup> was partly reduced by hydrogen at 180 °C during catalyst preparation.

The fine structures Pt-modified MnO<sub>2</sub> were further investigated using Mn (K-edge) and Pt (L-edge) EXAFS. Fig. 6a shows the normalized XANES spectra at the Mn K edge of MnO<sub>2</sub>, 0.1%Pt/MnO<sub>2</sub> and 0.5% Pt/MnO<sub>2</sub>, the Mn foil was also checked as reference. It is notable that the white line intensities increased with the increase of the Pt deposition amount, indicating the increase of AOS of Mn, which is consistent with the XPS results. Correspondingly, in the Fourier transforms (r space,

Fig. 6b) of the EXAFS data, there are two prominent peaks at 1.43 Å and 2.43 Å, corresponding to the Mn–O and Mn–Mn contributions, respectively [6]. The peak located at 1.43 Å slightly shifted to the right (Fig. 6c), indicating the Mn–O bond of Pt-deposited MnO<sub>2</sub> is longer than the Mn–O bond of MnO<sub>2</sub>. This result implies that the O atoms in the Pt-deposited MnO<sub>2</sub> lattice is more active than those in the MnO<sub>2</sub> lattice. Fig. 6d shows the normalized XANES spectra at the Pt L<sub>III</sub> edge of 0.5% Pt/MnO<sub>2</sub>, the used 0.5%Pt/MnO<sub>2</sub>, Pt foil and PtO<sub>2</sub>. The chemical state of Pt in MnO<sub>2</sub> is very close to that in PtO<sub>2</sub>. Furthermore, the change of Pt chemical state during catalytic oxidation process could be ignored. In the Fourier transforms (r space, Fig. 6e) of the EXAFS data, there is one

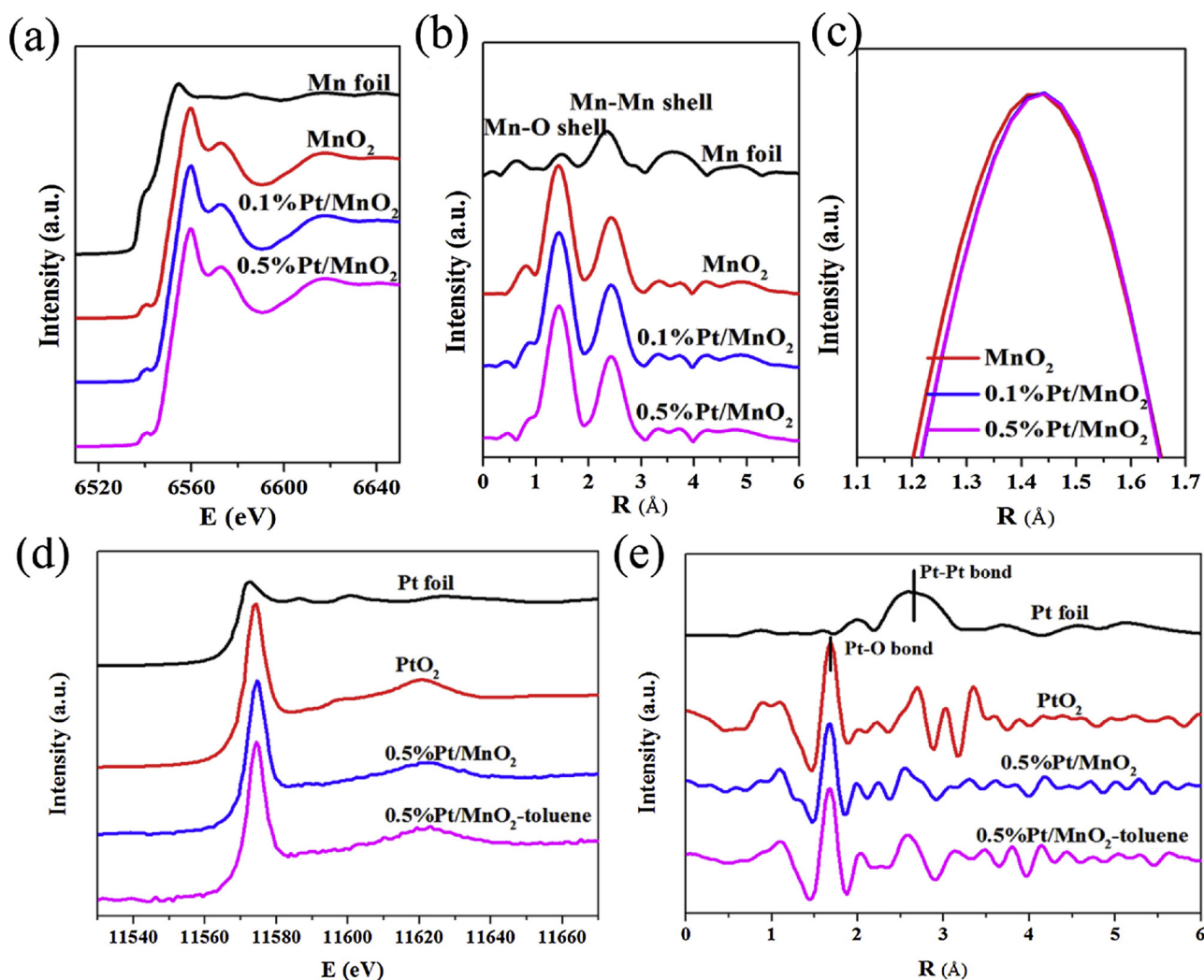


Fig. 6. (a) The normalized XANES spectra at the Mn K edge of Mn foil, MnO<sub>2</sub> and Pt<sub>x</sub>/MnO<sub>2</sub>; (b) The  $k^3$ -weighted Fourier transform spectra of Mn from EXAFS; (c) Magnification of the  $k^3$ -weighted Fourier transform spectra of Mn from EXAFS; (d) The normalized XANES spectra at the Pt L<sub>III</sub> edge of Pt foil, PtO<sub>2</sub>, 0.5%Pt/MnO<sub>2</sub>, and used 0.5%Pt/MnO<sub>2</sub>; (e) The  $k^3$ -weighted Fourier transform spectra of Pt from EXAFS.

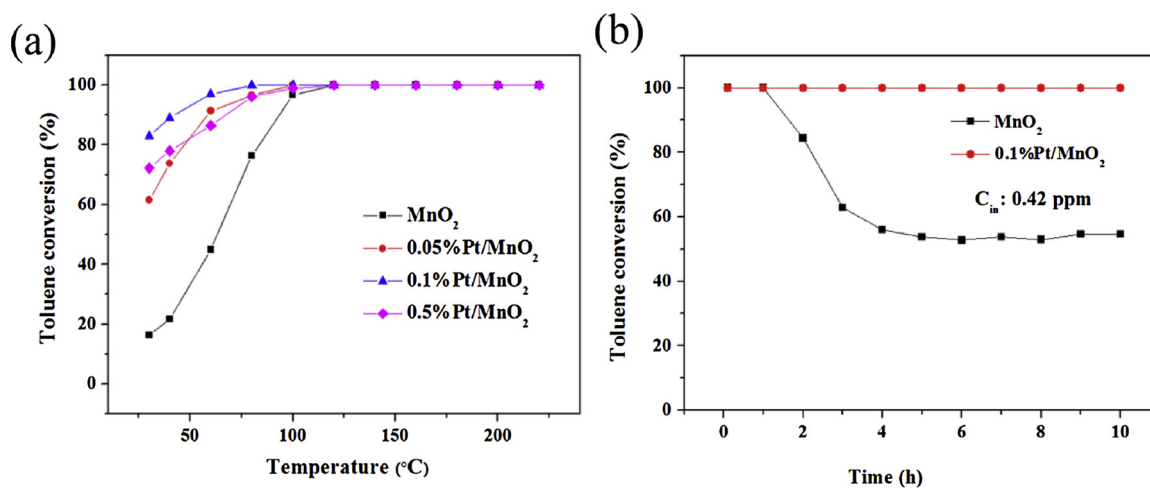


Fig. 7. (a) Temperature-dependent toluene conversion by MnO<sub>2</sub> and Pt-deposited MnO<sub>2</sub> catalysts (toluene inlet concentration: 10 ppm, 21% O<sub>2</sub>, N<sub>2</sub> as balance gas, GHSV: 60 L g<sup>-1</sup> h<sup>-1</sup>); (b) Toluene conversion by the 0.1%Pt/MnO<sub>2</sub> and MnO<sub>2</sub> at ambient temperature (toluene inlet concentration: 0.42 ppm, 21% O<sub>2</sub>, N<sub>2</sub> as balance gas, GHSV: 300 L g<sup>-1</sup> h<sup>-1</sup>).

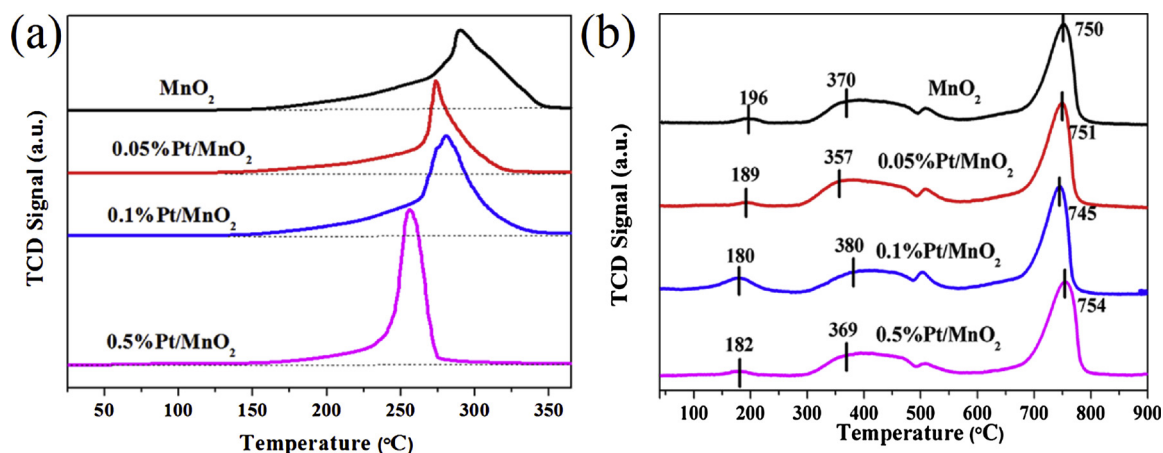


Fig. 8. (a)  $\text{H}_2$ -TPR and (b)  $\text{O}_2$ -TPD profiles of different samples.

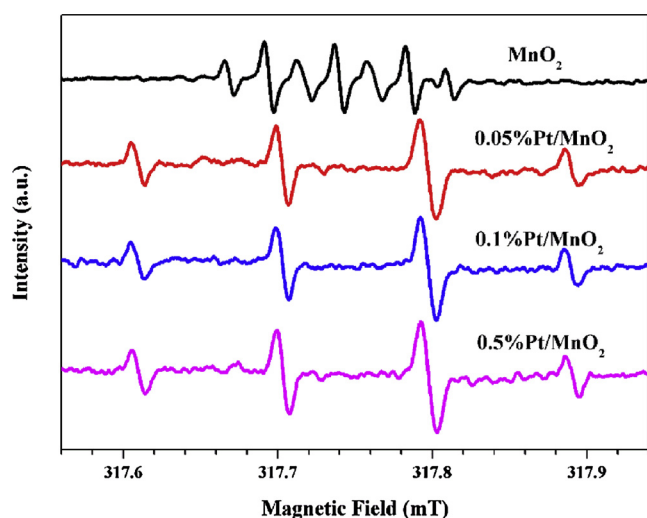


Fig. 9. ESR spectra of different  $\text{MnO}_2$  and Pt-deposited  $\text{MnO}_2$  samples in aqueous suspensions by using DMPO as trapping agent.

obvious peak at  $1.7 \text{ \AA}$  from the Pt-O contribution and a very weak peak at  $2.6 \text{ \AA}$  probably related to Pt-Mn bond. According to the EXAFS curve-fitting data of  $0.5\% \text{Pt}/\text{MnO}_2$ , the distance of first shell was  $2.0 \text{ \AA}$  with the corresponding coordination number of around 6.0, and the distance of second shell was  $2.97 \text{ \AA}$  with the corresponding coordination number of 4. The high coordination number and similar Pt-O bonding distance with  $\text{PtO}_2$  [19] suggest the strong metal-support interaction [16,19] in  $\text{MnO}_2$  nanosheets. These results confirmed the atomically dispersion of Pt atoms in the nanosheets of  $\text{MnO}_2$ , which is in good agreement with the HAADF results revealed above.

### 3.2. Catalytic activity for toluene oxidation and mechanism

We chose the toluene catalytic oxidation as a probe reaction to evaluate the catalytic activity of single-atom Pt-deposited  $\text{MnO}_2$ . Fig. 7a shows the temperature-dependent toluene conversion by different catalysts. Unmodified  $\text{MnO}_2$  itself also showed high activity for toluene conversion, achieving 100% conversion at  $120^\circ\text{C}$  for the inlet 10 ppm toluene under the GHSV of  $60 \text{ L g}^{-1} \text{ h}^{-1}$ . The deposition of single-atom Pt on  $\text{MnO}_2$  significantly increased the catalytic activity. Among them, the  $0.1\% \text{Pt}/\text{MnO}_2$  sample showed the best activity, achieving 100% conversion at  $80^\circ\text{C}$ . Particularly, all Pt-deposited  $\text{MnO}_2$  catalysts showed significant activity at room temperature. At  $28^\circ\text{C}$ , the  $0.1\% \text{Pt}/\text{MnO}_2$  sample achieved over 80% conversion of toluene at the GHSV of  $60 \text{ L g}^{-1} \text{ h}^{-1}$ . The turnover frequency (TOF) by deposited Pt atoms at

$28^\circ\text{C}$  was calculated according to the equation:  $\text{TOF} = x \times C_0 / [(m_{\text{catalyst}} \times \text{Pt content} / M_{\text{Pt}}) \times D]$ , where  $x$  is the conversion,  $C_0$  ( $\text{mol s}^{-1}$ ) is the initial toluene concentration per second,  $m_{\text{catalyst}}$  (g) is the mass of the catalyst,  $M_{\text{Pt}}$  (g/mol) is the molar weight of Pt, and  $D$  is the metal dispersion (100% dispersion was postulated) [40]. The TOF of  $0.1\% \text{Pt}/\text{MnO}_2$  for toluene degradation at  $28^\circ\text{C}$  was  $0.15 \text{ s}^{-1}$ , which is close to that in  $\text{Pt}/\text{Fe}_2\text{O}_3$  for the catalytic oxidation of benzene at  $160^\circ\text{C}$  [40]. It should be pointed out, the catalytic active sites for toluene include not only Pt atoms but also  $\text{MnO}_2$  and  $\text{Pt}/\text{MnO}_2$  interface, which may affect the calculated values of TOFs. Moreover, as shown in Fig. 7b, when we used the  $0.1\% \text{Pt}/\text{MnO}_2$  catalyst to treat low concentration toluene ( $0.42 \text{ ppm}$ ) at room temperature ( $28^\circ\text{C}$ ), which is close to those in the polluted indoor environment [41], it achieved 100% conversion under the high GHSV of  $300 \text{ L g}^{-1} \text{ h}^{-1}$  (the corresponding retention time  $\sim 0.24 \text{ s}$ ) during the whole 10-h test. As far as we know, it has never been reported that toluene could be degraded at the room temperature under very short retention time. Compared with the toluene degradation over unmodified  $\text{MnO}_2$  (Fig. 7b), we can find that the doping of single-atom platinum significantly improved the catalytic activity and stability at room temperature. So, it is very interesting to know why the single-atom Pt-deposited  $\text{MnO}_2$  owns excellent activity. What kind of active oxygen species is responsible for the toluene degradation at low temperature?

To explore the reason why single-atom  $\text{Pt}/\text{MnO}_2$  materials possess excellent catalytic activity for toluene oxidation at low temperature,  $\text{H}_2$ -TPR (Fig. 8a) and  $\text{O}_2$ -TPD (Fig. 8b) measurements were performed to evaluate the redox property of samples with different Pt content. It can be seen from the  $\text{H}_2$ -TPR profile (Fig. 8a), the addition of single atom Pt significantly decreased the initial reduction temperature from  $132$  to  $114^\circ\text{C}$ , indicating the samples with Pt became more reducible and reactive. The  $\text{O}_2$ -TPD spectra could be separated into three regions: surface active oxygen ( $< 260^\circ\text{C}$ ), sub-surface lattice oxygen ( $260^\circ\text{C}$ – $600^\circ\text{C}$ ) and bulk lattice oxygen ( $> 600^\circ\text{C}$ ), respectively. The  $0.1\% \text{Pt}/\text{MnO}_2$  have showed the lowest desorption temperature and the largest amount of labile oxygen among four catalysts.

We further investigated the radicals on the surface of as-prepared catalysts through ESR detection by using 5, 5-dimethyl-1-pyrroline N-oxide (DMPO) as the trapping agent. As shown in Fig. 9, in the aqueous suspension of DMPO and unmodified  $\text{MnO}_2$ , a characteristic seven-peak signal occurred, which can be ascribed to the 3-electron oxidation product of DMPO, i.e. the 5, 5-dimethyl-1-pyrrolidone-2-oxyl (DMPOX) [42]. The observation of this kind of ESR signal in pure or modified  $\text{MnO}_2$  was also reported by other researchers [43,44], and its generation could possibly be ascribed to oxidation of DMPO by peroxide species ( $\text{O}_2^{2-}$ ). While in the aqueous suspension of DMPO and any Pt-deposited  $\text{MnO}_2$ , the characteristic 1:2:2:1 four-peak signal of  $\text{DMPO}-\text{OH}^\bullet$  adducts [45] was detected, indicating the generation of

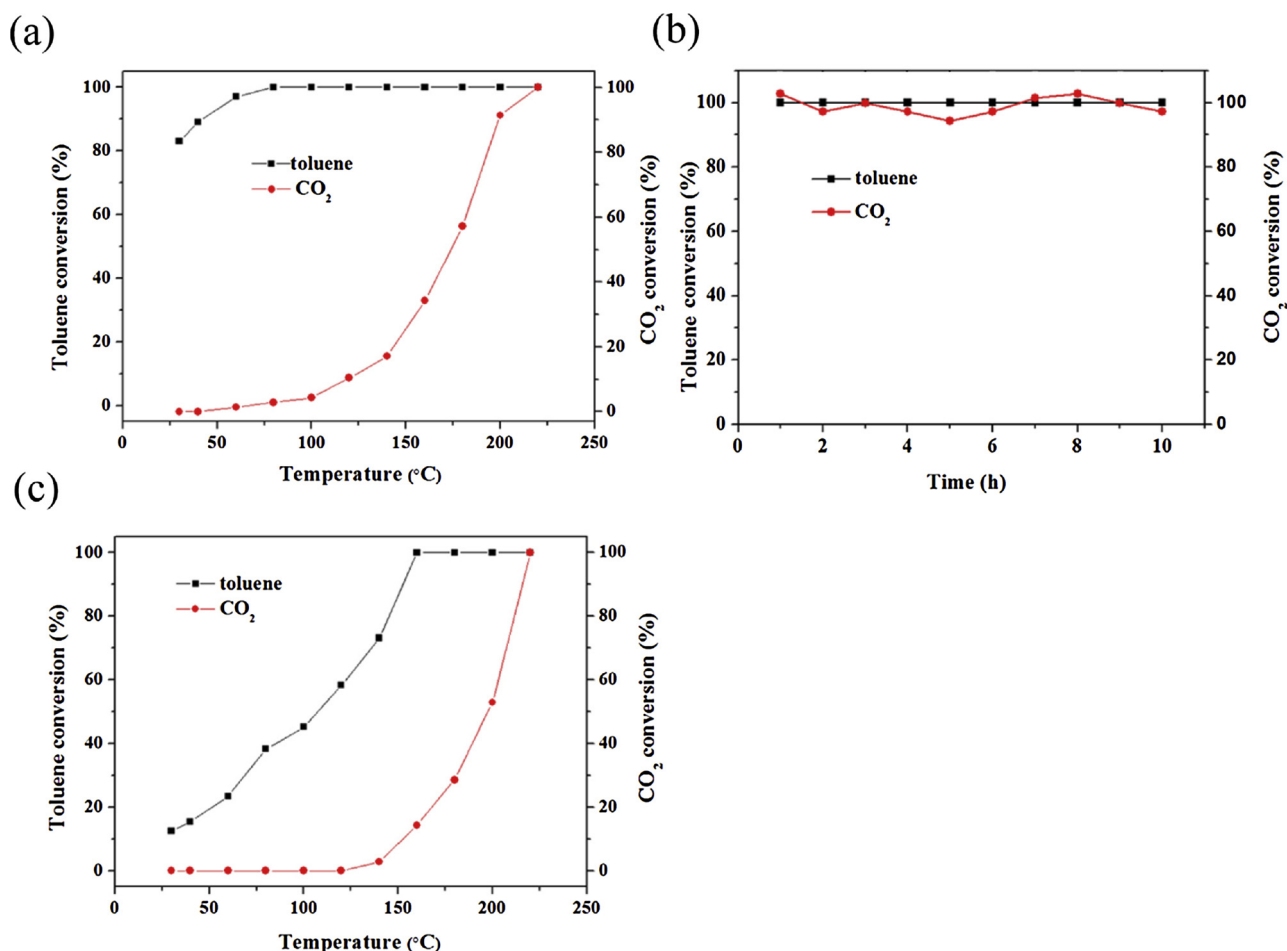


**Fig. 10.** (a) Conversion of toluene into CO<sub>2</sub> under different conditions by 0.1%Pt/MnO<sub>2</sub> catalyst (toluene inlet concentration: 10 ppm, 21% O<sub>2</sub>, N<sub>2</sub> as balance gas, GHSV: 60 L g<sup>-1</sup> h<sup>-1</sup>); (b) Stability text of 0.1%Pt/MnO<sub>2</sub> at 220 °C (toluene inlet concentration: 10 ppm, 21% O<sub>2</sub>, N<sub>2</sub> as balance gas, GHSV: 60 L g<sup>-1</sup> h<sup>-1</sup>); (c) Conversion of toluene into CO<sub>2</sub> under different temperatures by 0.1%Pt/MnO<sub>2</sub> catalyst (toluene inlet concentration: 100 ppm, 21% O<sub>2</sub>, N<sub>2</sub> as balance gas, GHSV: 48 L g<sup>-1</sup> h<sup>-1</sup>).

**Table 2**

Summary of the reported data on toluene decomposition over noble metal catalysts.

Catalyst	Noble metal content (wt %)	T <sub>50(toluene)</sub> (°C)	T <sub>100(toluene)</sub> (°C)	GHSV (L g <sup>-1</sup> h <sup>-1</sup> )	C <sub>toluene</sub> (ppm)	Refs.
Pt/γ-Al <sub>2</sub> O <sub>3</sub>	23.5%	–	225	30	100	[48]
Pt/TiO <sub>2</sub>	0.4%	–	200	30	300	[49]
Pt-Pd/MCM-41	0.2% + 0.1%	162	180	10	500	[50]
Au/MnO <sub>2</sub>	1.4%	125	300	40	170	[51]
Mn/R-SBA-15	0	217	240	15	500	[52]
Pt/MnO <sub>2</sub>	0.1%	110	160	48	100	This work

hydroxyl radicals (OH•) by Pt-deposited MnO<sub>2</sub>. It is well known, hydroxyl radical is a strong oxidant [46,47], which can oxidize most organic pollutants, so it can be understood that the single-atom Pt-deposited MnO<sub>2</sub> exhibited high activity to degrade toluene at room temperature.

Furthermore, we investigated the conversion of toluene into CO<sub>2</sub>. Fig. 10a shows the temperature-dependent conversion of toluene and its conversion into CO<sub>2</sub> in the presence of 0.1%Pt/MnO<sub>2</sub>. It can be seen that the corresponding conversion into CO<sub>2</sub> was much lower than the conversion of toluene at low temperatures, indicating toluene was not completely oxidized into CO<sub>2</sub> and some intermediates produced at low temperatures. Nevertheless, 0.1%Pt/MnO<sub>2</sub> realized complete oxidation of 10 ppm toluene into CO<sub>2</sub> at 220 °C under the GHSV of 60 L g<sup>-1</sup> h<sup>-1</sup>. We also investigated its stability at 220 °C within 10 h (Fig. 10b). Both toluene and CO<sub>2</sub> conversion kept stable at this temperature. To compare

the activity with catalysts reported in literatures, we also measured the activity of the 0.1%Pt/MnO<sub>2</sub> catalyst for high concentration toluene (100 ppm). As shown in Fig. 10c, under the GHSV of 48 L g<sup>-1</sup> h<sup>-1</sup>, the 50% and 100% toluene conversion temperature were 110 and 160 °C, respectively. In addition, the complete oxidation of toluene into CO<sub>2</sub> was realized at 220 °C. The comparison of as-prepared 0.1%Pt/MnO<sub>2</sub> catalyst with those reported in literatures was listed in Table 2 [48–52]. It can be found that the as-prepared single-atom Pt-deposited MnO<sub>2</sub> exhibited excellent activity for toluene conversion and its complete oxidation into CO<sub>2</sub>. Moreover, as shown in Fig. 6d, the Pt-deposited MnO<sub>2</sub> catalyst maintained the chemical state and dispersion of Pt after it was used in the oxidation process, indicating the satisfied structural stability of the single-atom Pt during the catalytic process.

To learn the intermediates formed during toluene oxidation process, we used the *in-situ* DRIFTS to observe the change of the catalyst surface.

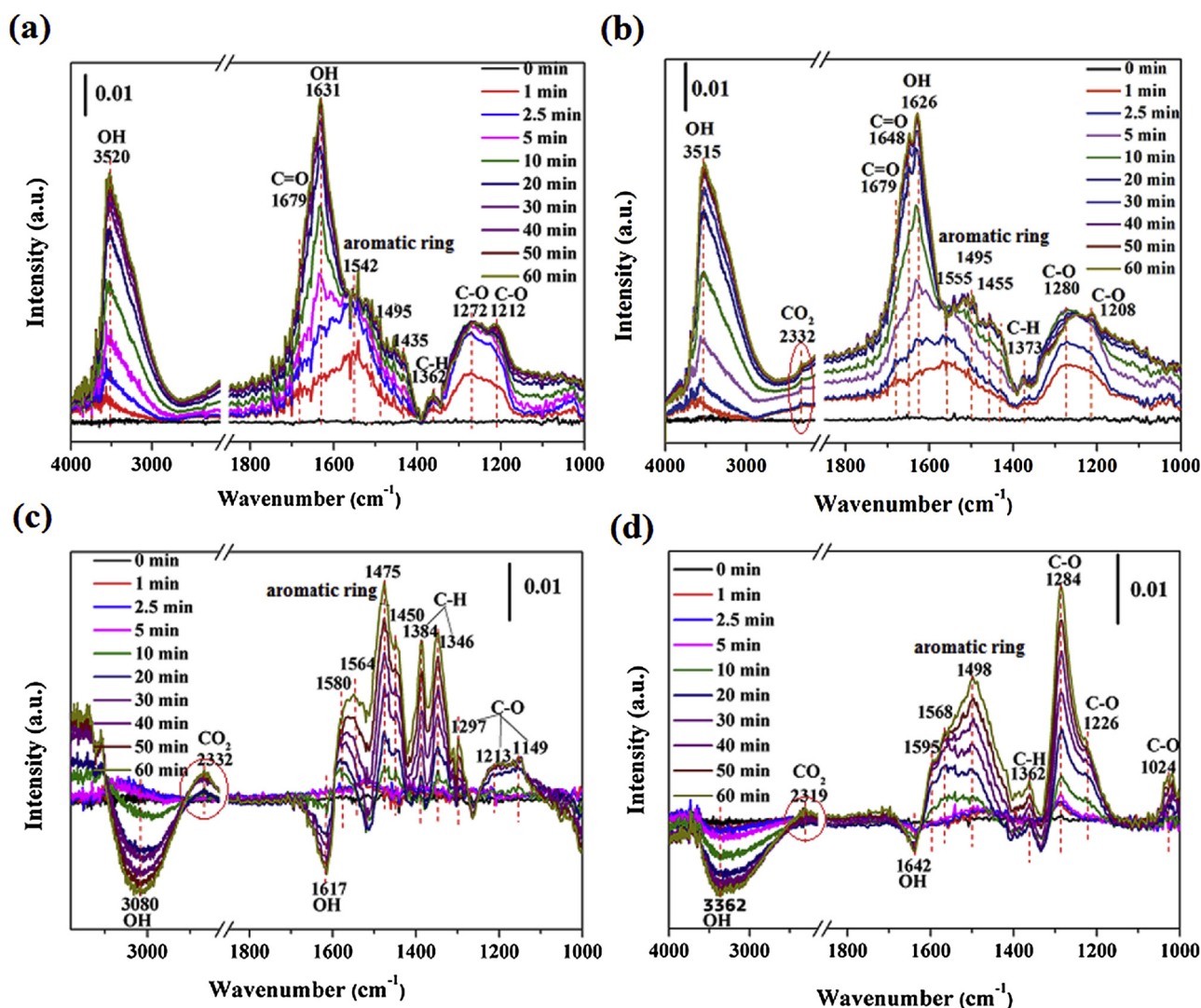


Fig. 11. In situ DRIFTS spectra of catalysts exposed to the flow of 15 ppm toluene. (a)  $\text{MnO}_2$  at room temperature; (b) 0.1%Pt/ $\text{MnO}_2$  at room temperature; (c) 0.1%Pt/ $\text{MnO}_2$  at 80 °C; (d) 0.1%Pt/ $\text{MnO}_2$  at 220 °C.

Fig. 11a shows the time-dependent DRIFTS of unmodified  $\text{MnO}_2$  exposed to the toluene flow at room temperature. It can be seen that the typical aromatic ring vibration peaks at  $1542\text{ cm}^{-1}$ ,  $1513\text{ cm}^{-1}$ ,  $1495\text{ cm}^{-1}$  immediately occurred and increased with time, indicating the rapid adsorption of toluene on the surface of the catalytic material [53–55]. The absorption peaks at  $1679\text{ cm}^{-1}$  belonged to the vibration of C=O bands, and the absorption peaks at  $1272\text{ cm}^{-1}$  and  $1212\text{ cm}^{-1}$  were the stretching vibrations of C–O. These absorption peaks can be ascribed to the carboxylic acid group [53], suggesting benzoate species were the key intermediate products during the catalytic process. The absorption peak at  $1362\text{ cm}^{-1}$  belonged to the bending vibration of C–H bands. In addition, there were two distinct peaks located at  $3600\text{--}2800\text{ cm}^{-1}$  and  $1631\text{ cm}^{-1}$ , which are ascribed to the stretching vibrations of OH group [5]. The OH groups may be contributed by the benzoate or water generated during the catalytic process. The in-situ DRIFTS of 0.1%Pt/ $\text{MnO}_2$  under the same conditions are shown in Fig. 11b, which were similar to the DRIFT spectra of  $\text{MnO}_2$ . However, the time that the main intermediates reaching equilibrium on the surface of 0.1%Pt/ $\text{MnO}_2$  was somewhat longer than that on the unmodified  $\text{MnO}_2$ . More importantly, it can be seen that the vibrational peak of  $\text{CO}_2$  appeared at  $2332\text{ cm}^{-1}$ , indicating that the loading of single-atom platinum promoted the decomposition of toluene into  $\text{CO}_2$  at room temperature [53].

We further observed the surface change of 0.1%Pt/ $\text{MnO}_2$  exposed to

the toluene flow at elevated temperatures. As shown in Fig. 11c, when the temperature was increased to 80 °C, the *in-situ* DRIFTS were much different from those at room temperature. The intensities of all peaks continuously increased with time, and the time needed to reaching sorption-desorption equilibrium became longer, indicating the faster decomposition of toluene and desorption of intermediates at elevated temperature. Moreover, the intensity of  $\text{CO}_2$  vibration peak at  $2332\text{ cm}^{-1}$  was much larger than that in Fig. 11b, indicating that the increase of temperature greatly promoted the complete decomposition of toluene into  $\text{CO}_2$ . In addition, the peak at  $3450\text{--}2500\text{ cm}^{-1}$  and  $1617\text{ cm}^{-1}$  ascribed to the vibration of hydroxyl group negatively increased with time. It has been reported that surface hydroxyl usually plays an important role in the process of catalytic oxidation [6]. Thus, the loss of surface hydroxyl group confirmed the accelerated reaction at elevated temperature. When the temperature was further increased to 220 °C (Fig. 11d), the vibration peak of  $\text{CO}_2$  at  $2332\text{ cm}^{-1}$  became weaker, indicating that  $\text{CO}_2$  desorbed very well at 220 °C. As a result, the catalytic active sites could be recovered for the next catalytic reaction turn, which confirmed the efficient and complete decomposition of toluene into  $\text{CO}_2$  by 0.1%Pt/ $\text{MnO}_2$  at 220 °C mentioned above.

#### 4. Conclusions

In this study, we successfully realized the atomically dispersion of Pt

on the MnO<sub>2</sub> nanosheets in the one-pot hydrothermal process utilizing the richness of Mn defects in birnessite-type MnO<sub>2</sub>. As-synthesized single-atom Pt-deposited MnO<sub>2</sub> showed excellent catalytic activity for toluene oxidation at low temperatures, achieving 100% conversion of indoor-level toluene at room temperature under the gas-hourly-space-velocity as high as 300 L g<sup>-1</sup> h<sup>-1</sup>. The deposition of single-atom Pt greatly activated surface oxygen species, and accordingly formed hydroxyl radicals (•OH) are thought to be responsible for efficient degradation of toluene at ambient and low temperatures. This study gives hope to catalytically remove indoor VOCs with the molecule-weights larger than formaldehyde at low temperatures, which is a great demand in the fields of indoor and industrial air treatment.

## Declaration of Competing Interest

The authors declare no competing financial interest.

## Acknowledgement

This work is financially supported by the National Natural Science Foundation of China (Nos. 51878374 and 21677083) and Suzhou-Tsinghua innovation guiding program (No. 2016SZ0104). Authors thank Mr. Lirong Zheng in Beijing Synchrotron Radiation Center for his help in data fitting.

## References

- [1] S. Gligorovski, J.P.D. Abbatt, An indoor chemical cocktail, *Science* 359 (2018) 632–633.
- [2] C.J. Jiang, D.D. Li, P.Y. Zhang, J.G. Li, J. Wang, J.G. Yu, Formaldehyde and volatile organic compound (VOC) emissions from particleboard: identification of odorous compounds and effects of heat treatment, *Build. Environ.* 117 (2017) 118–126.
- [3] L. Kirkeskov, T. Witterseh, L.W. Funch, E. Kristiansen, L. Molhave, M.K. Hansen, B.B. Knudsen, Health evaluation of volatile organic compound (VOC) emission from exotic wood products, *Indoor Air* 19 (2009) 45–57.
- [4] S.K. Brown, M.R. Sim, M.J. Abramson, C.N. Gray, Concentrations of volatile organic compounds in indoor air – a review, *Indoor Air* 4 (1994) 123–134.
- [5] S.P. Rong, P.Y. Zhang, Y.J. Yang, L. Zhu, J.L. Wang, F. Liu, MnO<sub>2</sub> framework for instantaneous mineralization of carcinogenic airborne formaldehyde at room temperature, *ACS Catal.* 7 (2017) 1057–1067.
- [6] J.L. Wang, P.Y. Zhang, J.G. Li, C.J. Jiang, R. Yunus, J. Kim, Room-temperature oxidation of formaldehyde by layered manganese oxide: effect of water, *Environ. Sci. Technol.* 49 (2015) 12372–12379.
- [7] M. Huang, X.L. Zhao, F. Li, L.L. Zhang, Y.X. Zhang, Facile synthesis of ultrathin manganese dioxide nanosheets arrays on nickel foam as advanced binder-free supercapacitor electrodes, *J. Power Sources* 277 (2015) 36–43.
- [8] S.P. Rong, K.Z. Li, P.Y. Zhang, F. Liu, J.Y. Zhang, Potassium associated manganese vacancy in birnessite-type manganese dioxide for airborne formaldehyde oxidation, *Catal. Sci. Technol.* 8 (2018) 1799–1812.
- [9] C.B. Zhang, F.D. Liu, Y.P. Zhai, H. Ariga, N. Yi, Y.C. Liu, K. Asakura, M. Stephanopoulos, H. He, Alkali-metal-promoted Pt/TiO<sub>2</sub> opens a more efficient pathway to formaldehyde oxidation at ambient temperatures, *Angew. Chem. Int. Ed.* 51 (2012) 9628–9632.
- [10] C.B. Zhang, H. He, K.I. Tanaka, Catalytic performance and mechanism of a Pt/TiO<sub>2</sub> catalyst for the oxidation of formaldehyde at room temperature, *Appl. Catal. B* 65 (2006) 37–43.
- [11] A.H. Mamaghani, F. Haghighat, C.S. Lee, Photocatalytic oxidation technology for indoor environment air purification: the state-of-the-art, *Appl. Catal. B* 203 (2017) 247–269.
- [12] X. Li, J. Xie, C.J. Jiang, J.G. Yu, P.Y. Zhang, Review on design and evaluation of environmental photocatalysts, *Front. Environ. Sci. Eng.* 12 (2018) 14–48.
- [13] F. Thevenet, L. Sivachandiran, O. Guaitella, C. Barakat, A. Rousseau, Plasma-catalyst coupling for volatile organic compound removal and indoor air treatment: a review, *J. Phys. D: Appl. Phys.* 47 (2014) 224011–224025.
- [14] H.B. Huang, D.Y.C. Leung, Complete oxidation of formaldehyde at room temperature using TiO<sub>2</sub> supported metallic Pd nanoparticles, *ACS Catal.* 1 (2011) 348–354.
- [15] M.S. Kamal, S.A. Razzak, M.M. Hossain, Catalytic oxidation of volatile organic compounds (VOCs)—a review, *Atmos. Environ.* 140 (2016) 117–134.
- [16] J.Y. Liu, Catalysis by supported single metal atoms, *ACS Catal.* 7 (2017) 34–59.
- [17] C.B. Zhang, Y.B. Li, Y.F. Wang, H. He, Sodium-promoted Pd/TiO<sub>2</sub> for catalytic oxidation of formaldehyde at ambient temperature, *Environ. Sci. Technol.* 48 (2014) 5816–5822.
- [18] H.H. Wei, K. Huang, D. Wang, R.Y. Zhang, B.H. Ge, J.Y. Ma, B. Wen, S. Zhang, Q.Y. Li, M. Lei, Iced photochemical reduction to synthesize atomically dispersed metals by suppressing nanocrystal growth, *Nat. Commun.* 8 (2017) 1490–1498.
- [19] B.T. Qiao, A.Q. Wang, X.F. Yang, L.F. Allard, Z. Jiang, Y.T. Cui, J.Y. Liu, J. Li, T. Zhang, Single-atom catalysis of CO oxidation using Pt<sub>1</sub>/FeOx, *Nat. Chem.* 3 (2011) 634–641.
- [20] M. Mosesdebusk, M. Yoon, L.F. Allard, D.R. Mullins, Z.L. Wu, X.F. Yang, G. Veith, G.M. Stocks, C.K. Narula, CO oxidation on supported single Pt atoms: experimental and ab initio density functional studies of CO interaction with Pt atom on θ-Al<sub>2</sub>O<sub>3</sub>(010) surface, *J. Am. Chem. Soc.* 135 (2013) 12634–12645.
- [21] J.W. Wan, W.X. Chen, C.Y. Jia, L.R. Zheng, J.C. Dong, X.S. Zheng, Y. Wang, W.S. Yan, C. Chen, Q. Peng, D.S. Wang, Y.D. Li, Defect effects on TiO<sub>2</sub> nanosheets: stabilizing single atomic site Au and promoting catalytic properties, *Adv. Mater.* 30 (2018) 1705369–1705377.
- [22] Y.P. Zhai, D. Pierre, R. Si, W.L. Deng, P. Ferrin, A.U. Nilekar, G.W. Peng, J.A. Herron, D.C. Bell, H. Saltsburg, M. Mavrikakis, M. Flytzanistephanopoulos, Alkali-stabilized Pt-OH<sub>x</sub> species catalyze low-temperature water-gas shift reactions, *Science* 329 (2010) 1633–1639.
- [23] M. Yang, J.L. Liu, S. Lee, B. Zugic, J. Huang, L.F. Allard, F.M. Stephanopoulos, A common single-site Pt(II)–O(OH)<sub>x</sub>-species stabilized by sodium on “Active” and “Inert” supports catalyzes the water-gas shift reaction, *J. Am. Chem. Soc.* 137 (2015) 3470–3473.
- [24] H.L. Fei, J.C. Dong, A.J.M. Josefine, G.L. Ye, N.M. Kim, E.L.G. Samuel, Z.W. Peng, Z. Zhu, F. Qin, J.M. Bao, M.J. Yacaman, P.M. Ajayan, D.L. Chen, J.M. Tour, Atomic cobalt on nitrogen-doped graphene for hydrogen generation, *Nat. Commun.* 6 (2015) 8668–8676.
- [25] C.H. Choi, M. Kim, H.C. Kwon, S.J. Cho, S. Yun, H.T. Kim, K.J.J. Mayrhofer, H. Kim, M. Choi, Tuning selectivity of electrochemical reactions by atomically dispersed platinum catalyst, *Nat. Commun.* 7 (2016) 10922–10931.
- [26] B.T. Qiao, J.X. Liang, A.Q. Wang, C.Q. Xu, J. Li, T. Zhang, J.Y. Liu, Ultrastable single-atom gold catalysts with strong covalent metal-support interaction (CMSI), *Nano Res.* 8 (2015) 2913–2924.
- [27] Z. Sihaib, F. Puleo, J.M. Garcia-Vargas, L. Retailleau, C. Descorme, L.F. Liotta, J.L. Valverde, S. Gil, A. Giroir-Fendler, Manganese oxide-based catalysts for toluene oxidation, *Appl. Catal. B* 209 (2017) 689–700.
- [28] F. Liu, M. Zeng, Y.Z. Li, Y. Yang, M.Y. Mao, X.J. Zhao, UV–vis–infrared light driven thermocatalytic activity of octahedral layered birnessite nanoflowers enhanced by a novel photoactivation, *Adv. Funct. Mater.* 26 (2016) 4518–4526.
- [29] R.M. Fang, W.J. Huang, H.B. Huang, Q.Y. Feng, M. He, J. Ji, B.Y. Liu, D.Y.C. Leung, Efficient MnOx/SiO<sub>2</sub>@AC catalyst for ozone-catalytic oxidation of gaseous benzene at ambient temperature, *Appl. Surf. Sci.* 470 (2019) 439–447.
- [30] L.J. Yan, Y.D. Gu, L.P. Han, P.L. Wang, H.R. Li, T.Y. Yan, S. Kuboon, L.Y. Shi, D.S. Zhang, Dual promotional effects of TiO<sub>2</sub>-decorated acid-treated MnOx octahedral molecular sieve catalysts for alkali-resistant reduction of NOx, *ACS Appl. Mater. Interfaces* 11 (2019) 11507–11517.
- [31] K.W. Zha, S.X. Cai, H. Hu, H.R. Li, T.T. Yan, L.Y. Shi, D.S. Zhang, In situ DRIFTS investigation of promotional effects of tungsten on MnOx-CeO<sub>2</sub>/meso-TiO<sub>2</sub> catalysts for NOx reduction, *J. Phys. Chem. C* 121 (2017) 25243–25254.
- [32] L. Miao, J.L. Wang, P.Y. Zhang, Review on manganese dioxide for catalytic oxidation of airborne, *Appl. Surf. Sci.* 466 (2019) 441–453.
- [33] J.B. Jia, P.Y. Zhang, L. Chen, Catalytic decomposition of gaseous ozone over manganese dioxides with different crystal structures, *Appl. Catal. B* 189 (2016) 210–218.
- [34] Y. Liu, W.J. Yang, P.Y. Zhang, J.Y. Zhang, Nitric acid-treated birnessite-type MnO<sub>2</sub>: an efficient and hydrophobic material for humid ozone decomposition, *Appl. Surf. Sci.* 442 (2018) 640–649.
- [35] C.T. Sun, Y.J. Zhang, S.Y. Song, D.F. Xue, Tunnel-dependent supercapacitance of MnO<sub>2</sub>: effects of crystal structure, *J. Appl. Crystallogr.* 46 (2013) 1128–1135.
- [36] Z.H. Huang, Y. Song, D.Y. Feng, Z. Sun, X. Sun, X.X. Liu, High mass loading MnO<sub>2</sub> with hierarchical nanostructures for supercapacitors, *ACS Nano* 12 (2018) 3557–3567.
- [37] Y.J. Xi, J.C. Ren, Design of a CO oxidation catalyst based on two dimensional MnO<sub>2</sub>, *J. Phys. Chem. C* 120 (2016) 24302–24306.
- [38] Q. Fu, H. Saltsburg, M. Flytzanistephanopoulos, Active nonmetallic Au and Pt species on ceria-based water-gas shift catalysts, *Science* 301 (2003) 935–938.
- [39] J. Liu, R. Younesi, T. Gustafsson, K. Edström, J.F. Zhu, Pt/a-MnO<sub>2</sub> nanotube: a highly active electrocatalyst for LiO<sub>2</sub> battery, *Nano Energy* 10 (2014) 19–27.
- [40] K. Yang, Y.X. Liu, J.D. Deng, X.T. Zhao, J. Yang, Z. Han, Z.Q. Hou, H.X. Dai, Three-dimensionally ordered mesoporous iron oxide-supported single-atom platinum: highly active catalysts for benzene combustion, *Appl. Catal. B* 244 (2019) 650–659.
- [41] C.J. Jiang, S.S. Li, P.Y. Zhang, J. Wang, Pollution level and seasonal variations of carbonyl compounds, aromatic hydrocarbons and TVOC in a furniture mall in Beijing, China, *Build. Environ.* 69 (2013) 227–232.
- [42] H. Wang, S.C. Chen, D.Y. Yong, X.D. Zhang, S. Li, W. Shao, X.S. Sun, B.C. Pan, Y. Xie, Giant electron-hole interactions in confined layered structures for molecular oxygen activation, *J. Am. Chem. Soc.* 139 (2017) 4737–4742.
- [43] W.J. Yang, Y.F. Zhu, F. You, L. Yan, Y.J. Ma, C.Y. Lu, P.Q. Gao, Q. Hao, W.L. Li, Insights into the surface-defect dependence of molecular oxygen activation over birnessite-type MnO<sub>2</sub>, *Appl. Catal. B* 233 (2018) 184–193.
- [44] Y.J. Yang, J.B. Jia, Y. Liu, P.Y. Zhang, The effect of tungsten doping on the catalytic activity of α-MnO<sub>2</sub> nanomaterial for ozone decomposition under humid condition, *Appl. Catal. A Gen.* 562 (2018) 132–141.
- [45] S. Gligorovski, R. Strekowski, S. Barabati, D. Vione, Environmental implications of hydroxyl radicals (•OH), *Chem. Rev.* 115 (2015) 13051–13092.
- [46] Y. Nosaka, A.Y. Nosaka, Generation and detection of reactive oxygen species in photocatalysis, *Chem. Rev.* 117 (2017) 11302–11336.
- [47] P.F. Xia, B.C. Zhu, B. Cheng, J.G. Yu, J.S. Xu, 2D/2D g-C<sub>3</sub>N<sub>4</sub>/MnO<sub>2</sub> nanocomposite as a direct Z-scheme photocatalyst for enhanced photocatalytic activity, *ACS Sustain. Chem. Eng.* 6 (2018) 965–973.
- [48] Z.B. Rui, C.Y. Chen, Y.B. Lu, H.B. Ji, Anodic alumina supported Pt catalyst for total oxidation of trace toluene, *Chin. J. Chem. Eng.* 22 (2014) 882–887.

- [49] Z.B. Rui, L.Y. Chen, H.Y. Chen, H.B. Ji, Strong metal-support interaction in Pt/TiO<sub>2</sub> induced by mild HCHO and NaBH<sub>4</sub> solution reduction and its effect on catalytic toluene combustion, *Ind. Eng. Chem. Res.* 53 (2014) 15879–15888.
- [50] X.R. Fu, Y. Liu, W.Y. Yao, Z.B. Wu, One-step synthesis of bimetallic Pt-Pd/MCM-41 mesoporous materials with superior catalytic performance for toluene oxidation, *Catal. Commun.* 83 (2016) 22–26.
- [51] A.G.M. Silva, T.S. Rodrigues, E.G. Candido, I.C. Freitas, A.H. Silva, H.V. Fajardo, R. Balzer, F. Janaina, J.F. Gomes, G.M. Assaf, D.C. Oliveira, N. Oger, S. Paul, R. Wojcieszak, P.H. Camargo, Combining active phase and support optimization in MnO<sub>2</sub>-Au nanoflowers: enabling high activities towards green oxidations, *J. Colloid Interface Sci.* 530 (2018) 282–291.
- [52] Y. Qin, Z.P. Qu, C. Dong, Y. Yang, N. Huang, Highly catalytic activity of Mn/SBA-15 catalysts for toluene combustion improved by adjusting the morphology of supports, *J. Environ. Sci. China* 76 (2019) 208–216.
- [53] H. Sun, Z.G. Liu, S. Chen, X. Quan, The role of lattice oxygen on the activity and selectivity of the OMS-2 catalyst for the total oxidation of toluene, *Chem. Eng. J.* 270 (2015) 58–65.
- [54] Y.B. He, Z.B. Rui, H.B. Ji, In situ DRIFTS study on the catalytic oxidation of toluene over V<sub>2</sub>O<sub>5</sub>/TiO<sub>2</sub> under mild conditions, *Catal. Commun.* 14 (2011) 77–81.
- [55] W.S. Chang, Y.M. Li, T. Chung, Y.S. Lin, C.M. Huang, Toluene decomposition using silver vanadate/SBA-15 photocatalysts: DRIFTS study of surface chemistry and recyclability, *Appl. Catal. A Gen.* 407 (2011) 224–230.